Applied Energy 414 (2026) 127848

Contents lists available at ScienceDirect

Applied Energy

journal homepage: www.elsevier.com/locate/apen

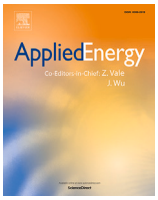

Privacy-preserving utilization of distribution system flexibility for enhanced TSO-DSO interoperability: A novel machine learning-based optimal power flow approach

Burak Dindar[a,*], Can Berk Saner[b], Hüseyin K. Çakmak[a], Veit Hagenmeyer[a]

[a] Institute for Automation and Applied Informatics, Karlsruhe Institute of Technology, Karlsruhe, 76344, Baden-Württemberg, Germany
[b] Electrical & Electronics Engineering, Ozyegin University, Istanbul, 34794, Turkiye

HIGHLIGHTS

- ML-based OPF enables privacy-preserving use of DS flexibility.
- DS constraints are modeled with ML trained only on non-sensitive data.
- Direct FPU dispatch via OPF is solved in a single communication round.
- A novel NN maps the DS feasible region with computational efficiency.
- Secure TSO–DSO collaboration is achieved while preserving data privacy.

ARTICLE INFO

Keywords:
Data privacy
Flexibility
Flexibility providing units
Machine learning
Neural network
Optimal power flow

ABSTRACT

Power system transformation makes distribution system (DS) flexibility crucial for efficient network management. Leveraging this flexibility requires interoperability between Transmission System Operators (TSOs) and Distribution System Operators (DSOs). However, data privacy concerns pose significant challenges to the effective utilization of this flexibility, since its integration often requires the exchange of sensitive information between TSOs and DSOs. For instance, in a conventional AC optimal power flow (OPF) problem, the TSO requires access to sensitive DSO information, such as network topology. To address this, we propose a machine learning (ML) based method in which DSOs train ML models using datasets that do not contain sensitive data, resulting in models defined by non-sensitive parameters. This prevents the transfer of sensitive information. Because models are trained solely on non-sensitive data, sensitive information remains protected against reverse engineering. After these trained models are shared by the DSOs with the TSO, the TSO can solve the OPF problem and determine flexibility-providing unit (FPU) dispatch in a single communication round. To achieve this, we introduce a tailored neural network (NN) architecture to efficiently represent the DS feasible region. To assess the effectiveness of the proposed method, we benchmark it against the standard AC-OPF on multiple DSs with meshed connections and multiple points of common coupling (PCCs) with varying voltage magnitudes. The numerical results show that the proposed method achieves competitive performance while preserving data privacy. Additionally, since this method directly determines the dispatch of FPUs, it eliminates the need for an additional disaggregation step. Overall, the proposed approach enables the effective utilization of DS flexibility in network management without compromising data privacy, thereby enhancing interoperability among stakeholders.

1. Introduction

With the rapid transformation of the power system, the number of flexibility-providing units (FPUs), such as distributed generators (DGs) connected to the distribution system (DS) is steadily increasing. The inherent fluctuations associated with DGs complicate the management not only of the DS but also of the transmission system (TS) [1]. On the other hand, the flexibility provided by DSs can be effectively

* Corresponding author.
Email addresses: burak.dindar@kit.edu (B. Dindar), canberk.saner@ozyegin.edu.tr (C.B. Saner), hueseyin.cakmak@kit.edu (H.K. Çakmak), veit.hagenmeyer@kit.edu (V. Hagenmeyer).

https://doi.org/10.1016/j.apenergy.2026.127848
Received 10 February 2025; Received in revised form 18 March 2026; Accepted 2 April 2026
Available online 7 April 2026

leveraged for the provision of ancillary services, contributing to the stability and reliability of the entire power system [2]. As the number of FPUs continues to rise, the necessity for effectively managing these flexibilities is becoming increasingly critical. However, the effective utilization of these flexibilities necessitates a high level of coordination between Transmission System Operators (TSOs) and Distribution System Operators (DSOs) [3].

In recent years, increasing the coordination between TSOs and DSOs and the utilization of DSs flexibility in ancillary services have garnered significant attention from researchers, leading to numerous studies focused on developing innovative coordination schemes [4–6]. These schemes typically require specific data exchanges between TSOs and DSOs in predefined formats. However, despite existing agreements governing such data transfers, the implementation of these coordination schemes in real-world projects faces numerous challenges and barriers [7]. One major issue is the unwillingness of stakeholders, such as TSOs and DSOs, to share essential data [8]. Current bilateral agreements often fail to address key concerns, such as data leakage, which can lead to the unintended disclosure of sensitive information. For instance, coordination schemes may expose DS system topology data (e.g., line parameters) or customer-specific load data, jeopardizing both commercially sensitive information and the privacy of individual customers. These concerns hinder interoperability and pose a significant challenge to the efficient operation of the power system [9]. Therefore, the primary objective of the present paper is to eliminate the exchange of commercially and personally sensitive data between TSOs and DSOs while ensuring overall data protection and privacy.

In this context, differential privacy (DP) has been investigated as a method for protecting sensitive data in power systems [10]. For example, DP has been applied to obscure transmission line and transformer parameters during data exchange in power grids [11]. Similarly, customer load data in distributed OPF has been protected using DP techniques [12]. In this method, noise is added to the data to prevent the exposure of sensitive information. While this approach enhances data protection, the introduction of noise can pose significant challenges in complex optimization algorithms such as OPF, potentially leading to infeasible solutions [13]. This, in turn, limits the effective utilization of FPU potential. As highlighted by Fioretto et al. [11], additional mechanisms are necessary to maintain high accuracy while preserving data privacy. However, implementing such mechanisms introduces extra computational overhead. Moreover, existing studies primarily focus on protecting specific types of data, without offering comprehensive solutions to safeguard all sensitive data simultaneously.

Another commonly used approach to ensure comprehensive data privacy in TSO-DSO interactions is the distributed OPF method [14]. In this approach, the OPF problem is decomposed into sub-problems to prevent the need for sharing complete grid models. However, it still requires the exchange of sensitive information such as complex voltages and/or active and reactive power flows at tie-lines between neighboring regions. While this method allows for the effective integration of FPUs from DSs into the TSO's OPF, it suffers from several limitations [15]. Firstly, the approach relies on iterative information exchanges between regions to achieve convergence, which significantly increases communication complexity. Secondly, as the number of DSOs in the system grows, the number of iterations and the time required for convergence rise considerably, posing scalability challenges [16]. Additionally, these methods often model FPUs using idealized rectangular PQ characteristics, failing to capture the diversity of real-world PQ capabilities.

Additionally, a wide range of approaches focuses on the concept of PQ capability charts to ensure data privacy in TSO-DSO coordination [17,18]. In this approach, the DSO calculates the aggregated flexibility at the TSO-DSO interface within the PQ domain [19,20]. This PQ region, often represented as a polygon, defines the feasible operating region (FOR) of the DS [21]. The TSO can then leverage these aggregated flexibilities for power system operations without the need to exchange sensitive data, such as the grid model [22,23].

In addition to the advantages related to data privacy, the PQ capability chart approach has a key limitation [24]: Specifically, the cost associated with any point on the PQ chart reflects the aggregate costs of various DGs, making it difficult to directly incorporate the cost implications of a TSO's selected point in the analysis [25]. Consequently, an additional disaggregation problem must be addressed to account for the individual costs of DGs [26]. For instance, in Polymeneas and Meliopoulos [27], a two-level hierarchical optimization scheme is proposed, where DGs are first aggregated, a multi-step optimal power flow (OPF) is performed, and then an optimization-based disaggregation problem is solved. Similarly, in Früh et al. [28], a top-down disaggregation process across voltage levels, based on a linear OPF model, is introduced and tested on a real distribution system. As illustrated, the PQ capability chart approach necessitates solving the disaggregation problem to effectively utilize aggregated flexibility in ancillary services, which introduces additional workload and requires iterative communication between TSOs and DSOs.

Another important aspect to consider regarding the PQ capability chart approach is the simplifications often employed in the method. In many studies, it is assumed that the DS is connected to the TS through a single point of common coupling (PCC), and radial test systems are utilized [29–31]. However, in reality, many DSs are operated in a meshed configuration, with multiple PCCs between TSOs and DSOs. Germany is a prominent example of this complexity; its 110 kV grid is meshed, connected to the TS via multiple PCCs, and managed by DSOs [32]. Moreover, a common assumption in the literature is that the voltage at the TSO-DSO interface, i.e., the PCC, remains constant [33]. However, in practical scenarios, the voltage at the PCC fluctuates depending on dispatch decisions. Assuming a constant voltage at the PCC can lead to an inaccurate assessment of DS flexibility potential, ultimately limiting its effective utilization. These simplifications and assumptions hinder the practical application of the PQ capability chart approach in real-world scenarios.

Considering the aforementioned challenges, our previous works [34,35] introduced a machine learning (ML)-based methodology to integrate DGs located within the DS into the OPF problem, which is solved by the TSO, while maintaining data privacy. Although various coordination schemes exist, ENTSO-E asserts that TSOs hold the primary responsibility for overall system security, while DSOs are tasked with ensuring the secure operation of their respective DSs [36]. In alignment with these responsibilities, our approach involves the DSO developing ML models that encapsulate the technical constraints of the DS based solely on the active and reactive power outputs of the DGs and the voltage magnitude at the PCC. By training ML models with this limited dataset, which comprises only information already known and shared between the TSO and DSO, commercially (e.g., system topology) and individually (e.g., customer load profiles) sensitive data is inherently protected, as these details are excluded from the dataset used for training. It is important to note that while ML models are generally susceptible to model inversion attacks, the proposed method ensures that even if reverse engineering is applied, no sensitive information is exposed, as the ML models are trained exclusively with non-sensitive data. Once trained, these ML models are transferred to the TSO, which subsequently utilizes them to solve the OPF problem, including the direct determination of DG dispatch within a single communication round. This approach not only guarantees data privacy by enabling the DSO to share only ML models trained on non-sensitive data, but also ensures that the overall system is managed by the TSO in compliance with ENTSO-E's operational framework. Simultaneously, the method considers the technical constraints of both the DS (through ML models) and the TS, facilitating a secure and coordinated operation.

In the present paper, we significantly enhance our previously proposed method by addressing the aforementioned challenges: The new approach extends the application of ML-based privacy-preserving OPF to not only a single DS but also to multiple DSs, even when there are multiple PCCs involved. Furthermore, we introduce a novel tailored neural

network (NN) to accurately and efficiently represent the feasible operating region of the DSs. To generate the necessary data for creating the ML models, the Latin hypercube sampling (LHS) method is employed. Additionally, to demonstrate the adaptability of the proposed method in handling diverse FPUs with varying PQ characteristics, we do not limit our study to DGs modeled with simple rectangular PQ charts. Instead, we also consider PQ charts with different characteristics. The LHS-based dataset generation is accordingly adjusted to reflect these varied characteristics. Finally, with the proposed method, instead of defining a PQ chart at the TSO-DSO interface, the flexibility of the DSs can be directly utilized by the TSO in power system management.

The key contributions of the present paper are as follows:

- Unlike conventional PQ capability chart approaches that require a disaggregation step, the proposed method directly integrates FPUs into the TSO's OPF formulation via ML models, enabling DG dispatch within a single communication round.
- In contrast to many existing studies that assume radial DSs connected through a single PCC and fixed PCC voltage, the proposed framework supports meshed DSs with multiple PCCs and treats PCC voltage as a decision variable to better capture available flexibility.
- While many PQ-chart-based methods assume idealized rectangular PQ capability regions, the proposed method supports FPUs with diverse and non-rectangular PQ characteristics.
- The tailored NN architecture enables efficient and accurate representation of the DSs' feasible operating region, improving computational performance.
- Overall, the proposed method enables the effective utilization of DS flexibility in TSO-level operation while preserving data privacy and respecting the operational limits of both TSs and DSs, thereby enhancing interoperability between TSOs and DSOs.

The rest of the paper is organized as follows: In Section 2, we present the proposed methodology. In Section 3, we introduce the dataset creation technique. Subsequently, in Section 4, we detail the representation of the DSs with ML models. Then, we benchmark the proposed method against the standard AC-OPF to evaluate its effectiveness in various case studies in Section 5. Finally, we present our conclusions in Section 6.

2. Overview of the proposed methodology

To set the notation in this paper, parameters are denoted by standard letters (a, A), and variables are represented using boldface letters ($\boldsymbol{a}$, $\boldsymbol{A}$), while sets are represented by calligraphic letters ($\mathcal{A}$). Matrices are denoted by uppercase (A), while scalar and (column) vector variables/parameters are presented in lowercase letters (a). Furthermore, functions are expressed as $A(\cdot)$. The n-th element of a vector a is denoted as $a^{(n)}$, and the n-th row of a matrix A is denoted as $A^{(n,:)}$. Moreover, the element at position (i, j) in a matrix is expressed as $A^{(i,j)}$. Finally, the symbols $\preceq$ and $\succeq$ are used for element-wise $\leq$ and $\geq$ comparisons, respectively.

2.1. Formulation of the standard AC-OPF

In the present paper, we consider an integrated power system with a total of n_{b} buses, comprising a transmission system (TS) with n_{g} conventional generators, and $n_{\mathrm{b,ts}}$ buses, as well as n_{ds} distribution systems (DSs), where the j-th DS contains $n_{\mathrm{dg},j}$ distributed generators (DGs). Note that some DSs have multiple points of common coupling (PCCs) with the TS. Following this consideration we can define the standard AC-OPF as follows:

$$\min_{\substack{\hat{\boldsymbol{v}},\hat{\boldsymbol{\theta}},\\ \check{\boldsymbol{p}}_{\mathrm{g}},\check{\boldsymbol{q}}_{\mathrm{g}},\\ \boldsymbol{p}_{\mathrm{dg},j},\\ \boldsymbol{q}_{\mathrm{dg},j}}} \quad \sum_{i=1}^{n_{\mathrm{g}}} C_i(\check{p}_{\mathrm{g}}^{(i)}) + \sum_{j=1}^{n_{\mathrm{ds}}} \sum_{k=1}^{n_{\mathrm{dg},j}} C_{jk}(\boldsymbol{p}_{\mathrm{dg},j}^{(k)}) \tag{1a}$$

$$\text{s.t.} \quad G_{\mathrm{P}}(\hat{\boldsymbol{v}},\hat{\boldsymbol{\theta}};\hat{Y}) + \hat{p}_{\mathrm{d}} - K\check{\boldsymbol{p}}_{\mathrm{g}} - \sum_{j=1}^{n_{\mathrm{ds}}} H_j \boldsymbol{p}_{\mathrm{dg},j} = 0, \tag{1b}$$

$$G_{\mathrm{Q}}(\hat{\boldsymbol{v}},\hat{\boldsymbol{\theta}};\hat{Y}) + \hat{q}_{\mathrm{d}} - K\check{\boldsymbol{q}}_{\mathrm{g}} - \sum_{j=1}^{n_{\mathrm{ds}}} H_j \boldsymbol{q}_{\mathrm{dg},j} = 0, \tag{1c}$$

$$G_{\mathrm{line}}(\hat{\boldsymbol{v}},\hat{\boldsymbol{\theta}};\hat{Y}) \preceq \hat{l}_{\mathrm{line,max}}, \tag{1d}$$

$$\hat{v}_{\min} \preceq \hat{\boldsymbol{v}} \preceq \hat{v}_{\max},\ \hat{\theta}_{\min} \preceq \hat{\boldsymbol{\theta}} \preceq \hat{\theta}_{\max}, \tag{1e}$$

$$\check{p}_{\mathrm{g,min}} \preceq \check{\boldsymbol{p}}_{\mathrm{g}} \preceq \check{p}_{\mathrm{g,max}},\ \check{q}_{\mathrm{g,min}} \preceq \check{\boldsymbol{q}}_{\mathrm{g}} \preceq \check{q}_{\mathrm{g,max}}, \tag{1f}$$

$$p_{\mathrm{dg},j,\min} \preceq \boldsymbol{p}_{\mathrm{dg},j} \preceq p_{\mathrm{dg},j,\max},\ \forall j \in \{1,..,n_{\mathrm{ds}}\}, \tag{1g}$$

$$q_{\mathrm{dg},j,\min} \preceq \boldsymbol{q}_{\mathrm{dg},j} \preceq q_{\mathrm{dg},j,\max},\ \forall j \in \{1,..,n_{\mathrm{ds}}\}. \tag{1h}$$

For clarity and ease of reference, we adopt the following notation: variables associated with the integrated system (including both TS and DS) are denoted with a hat ($\hat{\boldsymbol{a}}$), variables associated solely with the TS are denoted with an inverted hat ($\check{\boldsymbol{a}}$), and variables related exclusively to the DS are presented without a hat ($\boldsymbol{a}$). For example, $\hat{\boldsymbol{v}}$, represents the voltage magnitudes of all buses in the integrated system, while $\check{\boldsymbol{v}}$ refers only to the TS buses.

Following this convention, $\hat{\boldsymbol{v}}, \hat{\boldsymbol{\theta}}, \hat{p}_{\mathrm{d}}$, and $\hat{q}_{\mathrm{d}} \in \mathbb{R}^{n_{\mathrm{b}}}$ represent the vectors of bus voltage magnitude, voltage angle, active and reactive power demand vectors respectively, for the integrated system, which includes both TS and DSs. $\hat{Y} \in \mathbb{R}^{n_{\mathrm{b}} \times n_{\mathrm{b}}}$ denotes the bus admittance matrix. $\check{\boldsymbol{p}}_{\mathrm{g}}, \check{\boldsymbol{q}}_{\mathrm{g}} \in \mathbb{R}^{n_{\mathrm{b,ts}}}$ are the vectors of active and reactive power generation for the TS buses. K is the $n_{\mathrm{b}} \times n_{\mathrm{b,ts}}$ *transmission generation connection matrix* such that the element (t, v) is one if this element is located inside the TS, and zero otherwise. The vectors $\boldsymbol{p}_{\mathrm{dg},j}, \boldsymbol{q}_{\mathrm{dg},j} \in \mathbb{R}^{n_{\mathrm{dg}},j}$ correspond to the active and reactive power generation of the DGs in the j-th DS. H_j is the $n_{\mathrm{b}} \times n_{\mathrm{dg},j}$ *distributed generation connection matrix* such that the element (m, n) is one if the n-th DG of the j-th DS is located at bus m, and zero otherwise. It is important to note that the size of the vectors $\check{\boldsymbol{p}}_{\mathrm{g}}$ and $\check{\boldsymbol{q}}_{\mathrm{g}}$ corresponds to the number of TS buses, $n_{\mathrm{b,ts}}$, while the size of the vectors $\boldsymbol{p}_{\mathrm{dg},j}$ and $\boldsymbol{q}_{\mathrm{dg},j}$ corresponds to the number of DGs, $n_{\mathrm{dg},j}$.

Moreover, in (1a), the objective function minimizes the total cost of generation dispatch, including DGs. Here, $C_i(\cdot)$ represents the cost of active power generation at bus i, and similarly, $C_{jk}(\cdot)$ represents the cost of active power generation for the k-th DG in the j-th DS. Without loss of generality, we consider a standard quadratic cost function for both functions, expressed as $C_l(\boldsymbol{p}) = a_l \boldsymbol{p}^2 + b_l \boldsymbol{p} + c_l$. Note that, in this integrated system, we assume that the first n_{g} buses are associated with conventional generators for notational convenience. Eqs. (1b) and (1c) represent the active and reactive balance equations, where $G_P(\cdot)$ and $G_Q(\cdot)$ are the corresponding functions. In (1d), $G_{line}(\cdot)$ denotes the line apparent power flows, which are bounded by the line flow limit vector $\hat{l}_{\mathrm{line,max}}$. Finally, (1e)–(1h) establish the upper and lower bounds for the respective variables.

Examining Eq. (1), it becomes evident that the utilization of flexibility from DSs in network management requires access to sensitive data for the entire system. For instance, the admittance matrix $\hat{Y}$ encapsulates the topology of the system, while the demand vectors $\hat{p}_{\mathrm{d}}$ and $\hat{q}_{\mathrm{d}}$ contain load data. Typically, since the OPF problem is solved by the TSO, DSOs are reluctant to share such sensitive data with TSOs. To address this issue, in the present paper, we introduce a novel AC-OPF formulation designed to eliminate the need for sensitive data exchange between TSOs and DSOs. This new formulation allows for the effective use of DS flexibility in power system management while maintaining data privacy.

2.2. Formulation of the ML-based privacy-preserving AC-OPF

In our novel AC-OPF formulation, the primary goal is to prevent the exchange of sensitive data between TSOs and DSOs. To achieve this, we separate the DS-related variables and parameters from the integrated system. As previously described, we assume that there are n_{ds} distribution systems, and the j-th DS contains $n_{\mathrm{dg},j}$ distributed generators, where $j \in \{1, 2, \ldots, n_{\mathrm{ds}}\}$. We extend this setup by assuming that each distribution system j is connected to specific buses $\{s_{j,1}, s_{j,2}, \ldots, s_{j,r_j}\}$ (i.e., the points of common coupling (PCCs)) of the TS, where r_j denotes the number of PCCs for the j-th DS. These PCCs in the TS are treated as

empty buses, meaning these buses do not have any directly connected generators or loads.

Accordingly, we model each DS at the corresponding PCCs as dependent active and reactive power injections. These injections represent the power flows at the PCCs. For instance, a DS with a single PCC is modeled at that PCC, while a DS with multiple PCCs is represented by separate active and reactive power flows at each respective PCC. This representation depends on the vector $\boldsymbol{v}_j \in \mathbb{R}^{r_j}$, which consists of the voltage magnitudes at the PCCs $(s_{j,1}, s_{j,2}, \dots, s_{j,r_j})$ of the j-th DS. It also depends on the active and reactive power generation vectors of DGs, $\boldsymbol{p}_{\mathrm{dg},j}$ and $\boldsymbol{q}_{\mathrm{dg},j}$ for the j-th DS. For convenience, we concatenate these variables into a single vector $\boldsymbol{x}_j = \begin{bmatrix}\boldsymbol{v}_j^\top & \boldsymbol{p}_{\mathrm{dg},j}{}^\top & \boldsymbol{q}_{\mathrm{dg},j}{}^\top\end{bmatrix}^\top \in \mathbb{R}^{n_j}$, where $n_j = r_j + 2n_{\mathrm{dg},j}$. With this setup, we can define the proposed privacy-preserving AC-OPF as follows:

$$\min_{\substack{\check{\boldsymbol{v}},\check{\boldsymbol{\theta}},\\ \check{\boldsymbol{p}}_{\mathrm{g}},\check{\boldsymbol{q}}_{\mathrm{g}},\\ \boldsymbol{p}_{\mathrm{dg},j},\\ \boldsymbol{q}_{\mathrm{dg},j}}} \quad \sum_{i=1}^{n_{\mathrm{g}}} C_i(\check{\boldsymbol{p}}_{\mathrm{g}}^{(i)}) + \sum_{j=1}^{n_{\mathrm{ds}}} \sum_{k=1}^{n_{\mathrm{dg},j}} C_{jk}(\boldsymbol{p}_{\mathrm{dg},j}^{(k)}) \tag{2a}$$

$$\text{s.t.} \quad G_{\mathrm{p}}(\check{\boldsymbol{v}}, \check{\boldsymbol{\theta}}; \check{Y}) + \check{\boldsymbol{p}}_{\mathrm{d}} - \check{\boldsymbol{p}}_{\mathrm{g}} = 0, \tag{2b}$$

$$G_{\mathrm{Q}}(\check{\boldsymbol{v}}, \check{\boldsymbol{\theta}}; \check{Y}) + \check{q}_{\mathrm{d}} - \check{\boldsymbol{q}}_{\mathrm{g}} = 0, \tag{2c}$$

$$G_{\mathrm{line}}(\check{\boldsymbol{v}}, \check{\boldsymbol{\theta}}; \check{Y}) \preceq \check{I}_{\mathrm{line,max}}, \tag{2d}$$

$$\check{v}_{\min} \preceq \check{\boldsymbol{v}} \preceq \check{v}_{\max},\ \check{\boldsymbol{\theta}}_{\min} \preceq \check{\boldsymbol{\theta}} \preceq \check{\boldsymbol{\theta}}_{\max}, \tag{2e}$$

$$\check{p}_{\mathrm{g,min}} \preceq \check{\boldsymbol{p}}_{\mathrm{g}} \preceq \check{p}_{\mathrm{g,max}},\ \check{q}_{\mathrm{g,min}} \preceq \check{\boldsymbol{q}}_{\mathrm{g}} \preceq \check{q}_{\mathrm{g,max}}, \tag{2f}$$

$$P_{j,u}(\boldsymbol{x}_j) + \check{\boldsymbol{p}}_{\mathrm{g}}^{(s_{j,u})} = 0,\ \forall j \in \{1,..,n_{\mathrm{ds}}\}, \quad \forall u \in \{1,..,r_j\}, \tag{2g}$$

$$Q_{j,u}(\boldsymbol{x}_j) + \check{\boldsymbol{q}}_{\mathrm{g}}^{(s_{j,u})} = 0,\ \forall j \in \{1,..,n_{\mathrm{ds}}\}, \quad \forall u \in \{1,..,r_j\}, \tag{2h}$$

$$FR_j(\boldsymbol{x}_j) \preceq 0,\ \forall j \in \{1,..,n_{\mathrm{ds}}\}, \tag{2i}$$

$$x_{j,\min} \preceq \boldsymbol{x}_j \preceq x_{j,\max},\ \forall j \in \{1,..,n_{\mathrm{ds}}\}, \tag{2j}$$

$$\boldsymbol{x}_j = \begin{bmatrix}\boldsymbol{v}_j^\top\ \boldsymbol{p}_{\mathrm{dg},j}{}^\top\ \boldsymbol{q}_{\mathrm{dg},j}{}^\top\end{bmatrix}^\top, \forall j \in \{1,..,n_{\mathrm{ds}}\}. \tag{2k}$$

Examining Eqs. (2b)–(2f), it can be seen that these equations contain only TS-related variables. The DS-related variables are expressed through the functions defined in Eqs. (2g)–(2i). The functions $P_{j,u}(\boldsymbol{x}_j)$ and $Q_{j,u}(\boldsymbol{x}_j)$ are designed to represent DS-related variables in relation to the active and reactive power flow at the PCCs. Thanks to these functions, DSs are modeled as active and reactive power sources at the PCCs from the perspective of the TS. Note that the variables $\check{\boldsymbol{p}}_{\mathrm{g}}^{(s_{j,u})}$ and $\check{\boldsymbol{q}}_{\mathrm{g}}^{(s_{j,u})}$ represent the active and reactive power flow at the PCC, respectively, directed from the DS towards the TS.

The functions $FR_j(\boldsymbol{x}_j)$ are designed to represent the feasible region of the DSs. These functions ensure that technical constraints, such as line flow and voltage magnitude limits within the DS, are satisfied. Specifically, if $\boldsymbol{x}_j$ represents a feasible operating point that complies with all DS constraints, the condition $FR_j(\boldsymbol{x}_j) \preceq 0$ is satisfied. If this condition is not met, it indicates that $\boldsymbol{x}_j$ lies outside the feasible region. Moreover, (2j) defines the bounds for the DS-related variables. It should be noted that for each DS, only a single $FR_j(\boldsymbol{x}_j)$ function is created, regardless of the number of PCCs. However, for each DS, separate $P_{j,u}(\boldsymbol{x}_j)$ and $Q_{j,u}(\boldsymbol{x}_j)$ functions must be defined for each PCC.

In summary, we encapsulate non-sensitive DS-related variables within a specific set of functions to represent the technical constraints of the DS while preserving data privacy. These functions are constructed using ML models trained exclusively on non-sensitive DS-related variables, ensuring that sensitive data remains protected throughout the process. It should be emphasized that the ML-based functions do not arbitrarily replace the physical constraints of the DS. Instead, the datasets used to train the ML models are generated by evaluating candidate operating points using the physical DS model, where power flow feasibility and operational limits such as voltage magnitude and line flow constraints are explicitly verified. Based on these samples, the ML models inherently learn an implicit representation of the feasible operating region of the DS. Consequently, the learned function $FR_j(\boldsymbol{x}_j)$ acts as a surrogate constraint that approximates the feasible region. When embedded into the TSO-level OPF problem, this surrogate constraint ensures that candidate operating points remain consistent with the underlying DS operational limits without requiring the explicit DS network model.

The procedure for generating the datasets required to train the ML models is described in detail in Section 3. Subsequently, the NN-based construction of the $FR_j(\boldsymbol{x}_j)$ functions is introduced in Section 4.1, while the quadratic regression models used to obtain the $P_{j,u}(\boldsymbol{x}_j)$ and $Q_{j,u}(\boldsymbol{x}_j)$ functions are detailed in Section 4.2.

Fig. 1 illustrates the schematic representation of the proposed method. As outlined in previous sections, the OPF should be solved by TSOs. To facilitate this, the ML models and the cost functions of the DGs are shared with the TSO. By employing these ML models, the TSO can effectively solve the proposed ML-based privacy-preserving OPF as determined in (2). This approach allows the OPF to be solved and the dispatch decisions for the DGs to be determined in a single round of communication, without requiring any additional disaggregation processes. Consequently, the flexibility obtained from DSs can be utilized for various network management purposes in a cost-effective manner, while ensuring the protection of sensitive data and adhering to the technical constraints of both TSOs and DSOs.

2.3. Data privacy aspects of the proposed method

The proposed method explicitly addresses privacy concerns arising from the necessary data exchange between the TSO and DSOs. In a TSO-DSO coordination framework, potentially sensitive data include the internal topology of DSs, line parameters, customer load profiles, and detailed operational limits, all of which are known only to the DSOs. The DSO's primary objective is to protect this information from external entities. Here, a potential adversary may be either the TSO itself or a third party who gains access to this information.

In the proposed method, however, the ML models are trained exclusively using the PCC voltage magnitudes, which are already shared between both parties, and the active and reactive power outputs of the DGs, which are generally accessible to other stakeholders such as market operators. The detailed DS model that includes sensitive information is used only internally by the DSO during the dataset generation process. This ensures that the ML models are trained only on non-sensitive data.

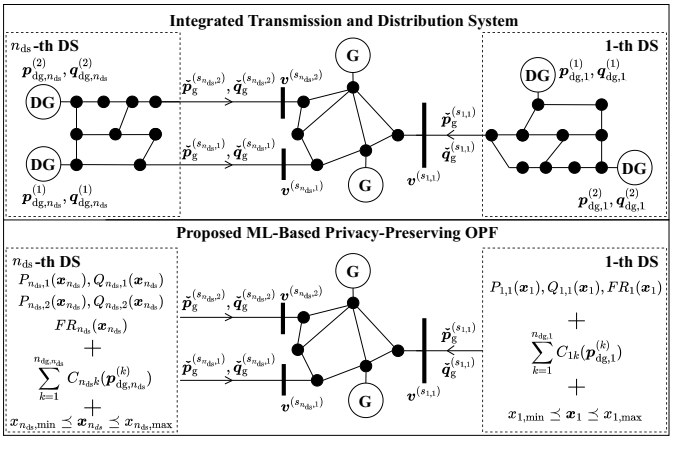

Fig. 1. Schematic representation of the proposed method.

Consequently, the training dataset is fundamentally decoupled from sensitive information such as network topology or physical line parameters. As a result, even if privacy attacks such as model inversion, membership inference, or attribute inference were to succeed, the ML models would not yield a direct or invertible mapping back to sensitive data.

This assumption ensures that the exchange of ML models enables interoperability between TSOs and DSOs without compromising confidentiality. By explicitly separating sensitive information from the training process, the framework prevents privacy violations while still allowing the TSO to utilize DS flexibility effectively.

Note that the proposed method follows the *data privacy by design* principle, unlike many privacy-preserving methods that rely on noise injection or data abstraction. Therefore, no explicit privacy-accuracy trade-off is introduced. Instead, the quality of the OPF solution primarily depends on the accuracy of the ML-based approximations. Accordingly, the case studies and benchmarks in this paper focus on demonstrating the operational performance of the proposed method, particularly with respect to approximation quality, including feasibility, cost-effectiveness and computational efficiency, rather than on simulating noise injection or privacy attacks.

3. Dataset creation

In the proposed method, we represent the technical constraints of the DSs using a set of functions developed through ML models. The effective training of these models necessitates a comprehensive dataset. To generate this dataset, we employ the Latin Hypercube Sampling (LHS) method [37]. LHS allows for sampling from a multidimensional distribution while maintaining the marginal probability distributions for each variable. This technique ensures efficient exploration of the entire range of each variable, even when the number of samples is relatively small.

To create the dataset, the DSO generates various operating points, represented by different values of $\boldsymbol{x}_j$, within the specified limits of these variables, as outlined in (2j). Particular attention must be given to the variables $\boldsymbol{p}_{\mathrm{dg},j}$ and $\boldsymbol{q}_{\mathrm{dg},j}$, as they define the PQ chart of the flexibility-providing units (FPUs). It is important to note that the DGs used in the present study can also be considered as FPUs.

In most studies, the PQ characteristics of FPUs are typically considered as rectangular (ideal or generic) [38] (see Fig. 2a). However, FPUs exhibit varying PQ characteristics, which are often modeled as convex polygons [39]. In Contreras and Rudion [40], rather than focusing on specific FPU shapes, such as triangular or square configurations, the methodology is demonstrated using arbitrary convex polygons. This approach illustrates the applicability of the method across diverse characteristics. Following this direction, the present paper also adopts arbitrary convex polygon PQ characteristics, thereby demonstrating the effectiveness of the proposed method for different FPU characteristics (see Fig. 2b).

In generating the dataset, we introduce a novel approach for sampling with LHS in scenarios involving arbitrary convex polygons. In this approach, the bounding rectangles formed by the $p_{\mathrm{dg},j,\min}$, $p_{\mathrm{dg},j,\max}$, $q_{\mathrm{dg},j,\min}$, and $q_{\mathrm{dg},j,\max}$ are used, and these bounding rectangles fully encapsulate the arbitrary convex polygons. Subsequently, LHS is applied within these bounding rectangles, enabling sampling from the entire arbitrary convex polygon that lies within the bounding rectangle.

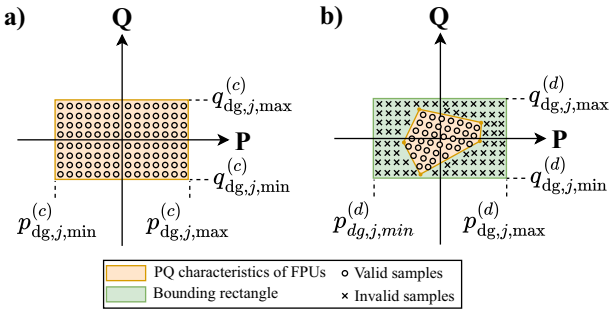

Fig. 2. Data sampling approach using LHS.

It is important to note that, as a natural consequence of this approach, some samples are taken from the area between the arbitrary polygon and the bounding rectangle. However, these samples do not represent feasible operating points. Fig. 2 illustrates the data sampling approach using LHS. Specifically, Fig. 2(a) illustrates a rectangular PQ characteristic, while Fig. 2(b) shows a PQ characteristic of a convex polygon along with its bounding rectangle. It also distinguishes between valid samples that fall within the convex polygon and invalid samples that are located in the region between the polygon and the bounding rectangle.

To ensure that only valid samples within the polygon are considered, an additional filtering approach is required. As is well known, convex polygons are characterized by a set of linear inequalities. Accordingly, these inequalities are expressed mathematically as follows:

$$A_{\mathrm{PQ},jk}\begin{bmatrix}\boldsymbol{p}^{(k)}_{\mathrm{dg},j} & \boldsymbol{q}^{(k)}_{\mathrm{dg},j}\end{bmatrix}^{\top} \preceq b_{\mathrm{PQ},jk}\,\forall j \in \{1,..,n_{\mathrm{ds}}\}\text{and}\,\forall k \in \{1,..,n_{\mathrm{dg},j}\}, \tag{3}$$

where $A_{\mathrm{PQ},jk} \in \mathbb{R}^{n_{\mathrm{v},jk}\times 2}$ represents the matrix of coefficients, while $b_{\mathrm{PQ},jk} \in \mathbb{R}^{n_{\mathrm{v},jk}}$ is the vector of constants. Also, $n_{\mathrm{v},jk}$ indicates the number of vertices that define the convex polygon for a given DG. Note that, for DGs with rectangular characteristics, the vertices are determined by the $p_{\mathrm{dg},j,\min}$, $p_{\mathrm{dg},j,\max}$, $q_{\mathrm{dg},j,\min}$ and $q_{\mathrm{dg},j,\max}$ values. After defining these linear inequalities, they can be incorporated into the OPF problem defined in (2) to ensure that invalid samples, which lie between the convex polygon and the bounding rectangle, are identified as infeasible. To achieve this, we can extend the OPF problem as follows:

$$\begin{aligned}&\min \quad (2a)\\ &\text{s.t.} \quad (2b)\text{–}(2k),\\ &\qquad (3).\end{aligned} \tag{4}$$

This ensures that invalid samples are appropriately classified as infeasible, allowing only valid samples to be evaluated. This approach facilitates dataset generation using standard LHS without the need for additional sampling techniques. Consequently, the proposed method can effectively handle FPUs with arbitrary convex polygon characteristics beyond rectangular ones. Furthermore, since the FPUs characteristics are represented by linear inequalities, they can be integrated into the OPF problem in a computationally efficient manner.

Overall, each operating point $\boldsymbol{x}_j$ generated by LHS is assessed based on the security limits of the DSs using power flow analysis. Based on this evaluation, the operating points are classified as either feasible or infeasible. Subsequently, datasets are compiled consisting of feasible instances $\mathcal{F}$ and infeasible instances $\mathcal{I}$.

4. Representation technical constraints of the distribution systems with machine learning models

After generating the dataset, ML models are trained to construct the previously defined functions. Specifically, we introduce a novel, tailored NN classification model to construct the $FR_j(\boldsymbol{x}_j)$ functions. In addition, quadratic regression models are employed to construct $P_{j,u}(\boldsymbol{x}_j)$ and $Q_{j,u}(\boldsymbol{x}_j)$ functions.

It is important to recall that the $FR_j(\boldsymbol{x}_j)$ functions determine the feasible region of the DSs by incorporating their technical constraints. In this way, they ensure that all operational limits of the DSs are satisfied in any dispatch of the DGs. Meanwhile, the functions $P_{j,u}(\boldsymbol{x}_j)$ and $Q_{j,u}(\boldsymbol{x}_j)$ establish the coupling between DS-related variables and the active/reactive power at the PCCs. Consequently, from the perspective of the TS, each DS can be effectively modeled as an equivalent active and reactive power source at its corresponding PCC.

4.1. NN-guided polytope representation of feasible region

In this section, we model the functions $FR_j(\boldsymbol{x}_j)$ in the form of a convex polytope, ensuring that the condition $FR_j(\boldsymbol{x}_j) \preceq 0$ is satisfied. To construct this model, we utilize a previously generated dataset that consists of a finite number of feasible and infeasible instances i.e., $\mathcal{F}$ and $\mathcal{I}$. Following this, we can describe the function as follows:

$$FR_j(\boldsymbol{x}_j) = A_{\mathrm{FR},j}\boldsymbol{x}_j - b_{\mathrm{FR},j}. \tag{5}$$

To construct a convex polytope that encompasses all feasible instances, we need to determine a matrix $A_{\mathrm{FR},j} \in \mathbb{R}^{n_{\mathrm{f},j}\times n_j}$ and a vector $b_{\mathrm{FR},j} \in \mathbb{R}^{n_{\mathrm{f},j}}$. This formulation ensures that all feasible instances $\boldsymbol{x}_j \in \mathcal{F}$ satisfy the inequality $A_{\mathrm{FR},j}\boldsymbol{x}_j \preceq b_{\mathrm{FR},j}$, while all infeasible instances $\boldsymbol{x}_j \in \mathcal{I}$ do not satisfy this inequality, i.e., $A_{\mathrm{FR},j}\boldsymbol{x}_j \npreceq b_{\mathrm{FR},j}$. Note that, $n_{\mathrm{f},j}$ represents the number of facets of the polytope, assuming that there is no redundancy in $A_{\mathrm{FR},j}\boldsymbol{x}_j \preceq b_{\mathrm{FR},j}$.

The next step in constructing the polytope involves determining under what circumstances an operating point x_j satisfies the defined inequality. We consider x_j to satisfy the inequality if and only if every element of z is less than or equal to zero, where $z = A_{\mathrm{FR},j}x_j - b_{\mathrm{FR},j}$. As a result, $\max(z) \leq 0$ indicates that x_j lies inside the polytope, making it a feasible point. On the contrary, if at least one element of x_j is strictly greater than zero, this implies $\max(z) > 0$, meaning that x_j is outside the polytope and therefore an infeasible instance. To better understand this polytope, Fig. 3 provides a schematic representation with $n_{\mathrm{f},j} = 6$, where feasible instances are depicted by – and infeasible instances by +.

After determining the approach to assess whether a given operating point x_j lies inside or outside the polytope, the next crucial step is to define the appropriate parameters $A_{\mathrm{FR},j}$ and $b_{\mathrm{FR},j}$. To achieve this, we leverage a novel tailored NN architecture specifically designed for this purpose. Upon training, the weights and biases of this NN model are directly mapped to the parameters $A_{\mathrm{FR},j}$ and $b_{\mathrm{FR},j}$. In this framework, feasible instances are labeled as Class 0, and infeasible instances as Class 1. The proposed NN architecture can be mathematically represented as follows:

$$\boldsymbol{o}_j = W_j\boldsymbol{x}_j + b_j, \tag{6a}$$

$$\boldsymbol{f}_j = \max(\boldsymbol{o}_j), \mathbb{Z} \tag{6b}$$

$$\boldsymbol{y}_j = \mathrm{sigmoid}(\boldsymbol{f}_j). \tag{6c}$$

Eq. (6) describes a feed-forward architecture. Firstly, (6a) represents a hidden layer with $n_{h,j}$ nodes, where $W_j \in \mathbb{R}^{n_{\mathrm{h},j}\times n_j}$ denotes the weight matrix and $b_j \in \mathbb{R}^{n_{\mathrm{h},j}}$ denotes the bias vector. In (6b), instead of using a standard activation function, the output of the hidden layer $\boldsymbol{o}_j \in \mathbb{R}^{n_{\mathrm{h},j}}$ is processed by a max aggregator function, resulting in $\boldsymbol{f}_j \in \mathbb{R}$. Then, $\boldsymbol{f}_j$ is passed through the sigmoid activation in (6c), producing the final output $\boldsymbol{y}_j \in [0, 1]$, which can be interpreted as the probability of infeasibility of a given input $\boldsymbol{x}_j$. Fig. 4 shows the architecture of the proposed NN. Finally, to train the NN, we employ the standard binary cross-entropy loss function.

As the final step, the relationship between the weights W_j and biases b_j of the NN and matrix $A_{\mathrm{FR},j}$ and vector $b_{\mathrm{FR},j}$ needs to be established.

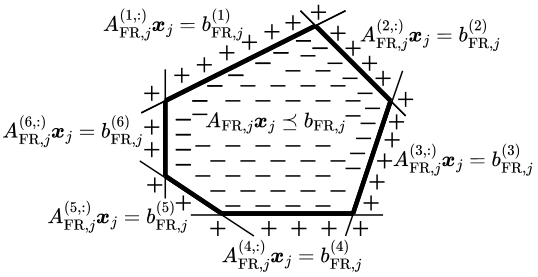

Fig. 3. Schematic representation of the polytope.

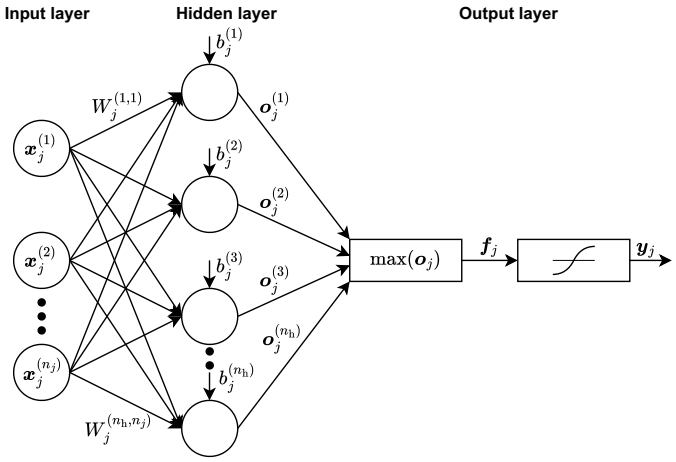

Fig. 4. The architecture of the novel tailored NN.

According to (6), a sample $\boldsymbol{x}_j$ is classified as feasible if $\max(W_j\boldsymbol{x}_j + b_j) \leq 0$ and as infeasible if $\max(W_j\boldsymbol{x}_j + b_j) > 0$. This implies that the decision region for feasible samples is defined by $W_j\boldsymbol{x}_j \preceq -b_j$. Thus, the desired polytope can be defined by setting $A_{\mathrm{FR},j} = W_j$ and $b_{\mathrm{FR},j} = -b_j$. Note that, the number of hidden nodes $n_{\mathrm{h},j}$ provides an upper bound on the number of facets of the polytope (though this is only an upper bound, as some rows of $W_j\boldsymbol{x}_j \preceq -b_j$ may be redundant).

After obtaining $A_{\mathrm{FR},j}$ and $b_{\mathrm{FR},j}$ from the NN, one critical aspect in accurately mapping the feasible region by using the polytope approach is the possibility of misclassification. Incorrectly classifying a feasible point as infeasible may only lead to economic losses, while misclassifying an infeasible point as feasible can result in significant issues within the power system. To mitigate this risk, we introduce a *conservativeness parameter* $c_{\mathrm{FR},j}$, which is directly embedded into the inequality constraints of the polytope, modifying its formulation as:

$$A_{\mathrm{FR},j}\boldsymbol{x}_j \preceq b_{\mathrm{FR},j} - c_{\mathrm{FR},j}. \tag{7}$$

Assigning a positive value to $c_{\mathrm{FR},j}$ shifts the polytope's boundaries inward, resulting in a smaller but more reliable feasible region. This adjustment reduces the risk of misclassifying infeasible points as feasible. Naturally, the choice of $c_{\mathrm{FR},j}$ entails a trade-off: larger values increase conservativeness, but at the expense of excluding some feasible points, thereby slightly increasing the total cost. Selecting this parameter appropriately is therefore crucial. By employing this strategy, we can represent the non-convex feasible area as a conservative convex polytope, ensuring a more reliable representation of the feasible region. Finally, by incorporating the constraint $A_{\mathrm{FR},j}\boldsymbol{x}_j \preceq b_{\mathrm{FR},j} - c_{\mathrm{FR},j}$ into the OPF problem as specified in (2i), the feasible region of the DS can be effectively approximated. Utilizing such a polytope allows the OPF to be implemented in a computationally efficient and privacy-preserving manner.

4.2. Quadratic regression-based power flow approximator

After defining the feasible region of the DSs, we focus on defining the functions $P_{j,u}(\boldsymbol{x}_j)$ and $Q_{j,u}(\boldsymbol{x}_j)$. These functions are designed to map the DS-related variables $\boldsymbol{x}_j$ to the active and reactive power flows at the PCCs, respectively. Considering the inherent quadratic relationship between power injections and system losses [41], we select a quadratic regression model to define these mappings. Accordingly, these functions can be described as follows:

$$P_{j,u}(\boldsymbol{x}_j) = \boldsymbol{x}_j^\top A_{\mathrm{P},j,u}\boldsymbol{x}_j + b_{\mathrm{P},j,u}^\top\boldsymbol{x}_j + c_{\mathrm{P},j,u}, \tag{8a}$$

$$Q_{j,u}(\boldsymbol{x}_j) = \boldsymbol{x}_j^\top A_{\mathrm{Q},j,u}\boldsymbol{x}_j + b_{\mathrm{Q},j,u}^\top\boldsymbol{x}_j + c_{\mathrm{Q},j,u}, \tag{8b}$$

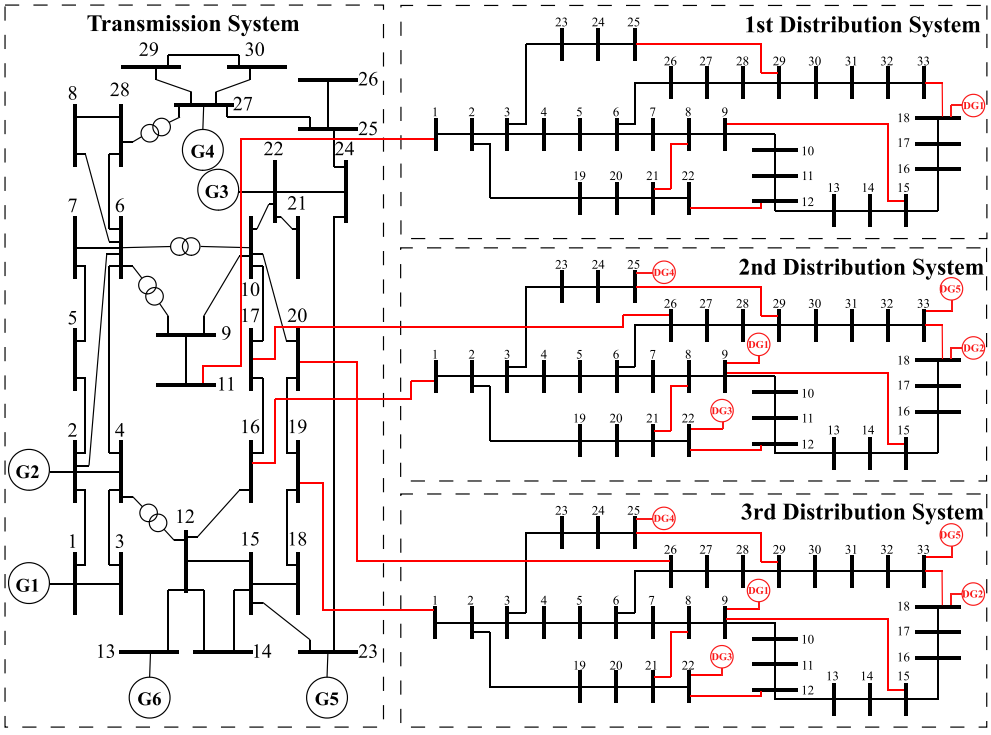

Fig. 5. Single-line diagram of the integrated power system, where the modifications introduced to the network are highlighted in red.

where $A_{\mathrm{P},j,u}, A_{\mathrm{Q},j,u} \in \mathbb{R}^{n_j \times n_j}$, and $b_{\mathrm{P},j,u}, b_{\mathrm{Q},j,u} \in \mathbb{R}^{n_j}$, and $c_{\mathrm{P},j,u}, c_{\mathrm{Q},j,u} \in \mathbb{R}$ represent the model parameters, which are determined through standard ML training procedures.

To train the quadratic regression models, we use $\boldsymbol{x}_j$ as input, active and reactive power at the PCCs, i.e., $\check{\boldsymbol{p}}_{\mathrm{g}}^{(s_{j,u})}$ and $\check{\boldsymbol{q}}_{\mathrm{g}}^{(s_{j,u})}$ as output of the models. The values of $\check{\boldsymbol{p}}_{\mathrm{g}}^{(s_{j,u})}$ and $\check{\boldsymbol{q}}_{\mathrm{g}}^{(s_{j,u})}$ are derived from power flow calculations. Note that, while both feasible instances $\mathcal{F}$ and infeasible instances $\mathcal{I}$ are utilized in the NN models, only feasible instances $\mathcal{F}$ are employed for training the quadratic regression models. This ensures that the regression models are trained exclusively on physically valid operating points, thereby avoiding the risk of learning invalid relationships introduced by infeasible samples. Upon completion of the training process, these functions accurately represent the relationship between DG-related variables and the corresponding power flows at the PCCs.

5. Case studies and discussion

In the present paper, the performance of the proposed method is evaluated by comparing it with the traditional AC-OPF, which does not consider data privacy. The evaluation process involves several steps: first, a suitable power system is established, followed by the generation of a comprehensive dataset. ML models are then trained using this dataset, and their approximation accuracy is assessed. Finally, the effectiveness of the proposed method is examined through extensive case studies.

The primary simulation environment for this study is MATLAB, where we utilize MATPOWER [42] with the KNITRO solver [43] for performing AC-OPF calculations. ML models are developed and trained using TensorFlow/Keras [44,45]. The case studies are conducted on a PC equipped with an Intel Core i7-10700K CPU @ 3.80 GHz and 32 GB RAM.

5.1. Power system creation

To create an appropriate integrated transmission and distribution system, we employ the IEEE 30-bus test system as the TS, and three IEEE 33-bus test systems as the DSs. Fig. 5 shows the integrated power system configuration. For all DSs, the normally open lines are closed, converting the systems into meshed grids to assess the effectiveness of the proposed method in meshed grids. The first DS is connected to the 11th bus of the TS (i.e., $s_{1,1} = 11$) through a single PCC, and includes only one DG. This setup is designed such that the first DS is represented in a three-dimensional space (i.e., $\boldsymbol{x}_1 \in \mathbb{R}^3$), enabling the proposed method to be visualized within three dimensions.

To demonstrate the effectiveness of the proposed method in a more complex system, five DGs are integrated into the second DS. Additionally, as is commonly observed in real-world scenarios, this DS is connected to the TS through two PCCs located at the 16th and 17th buses of the TS (i.e., $s_{2,1} = 16$ and $s_{2,2} = 17$), effectively showcasing the scenario involving multiple PCCs. The third DS demonstrates the effectiveness of the proposed method on FPUs with varying PQ characteristics. To achieve this, the same topology as the second DS is employed, but instead of DGs with only rectangular PQ charts as in the first two DSs, this system incorporates DGs with varying convex polygon PQ characteristics, as illustrated in Fig. 6. This setup demonstrates that the proposed method maintains high performance regardless of the specific PQ characteristics. Additionally, the third DS is connected to the TS through two PCCs at the 19th and 20th buses of the TS (i.e., $s_{3,1} = 19$ and $s_{3,2} = 20$). Furthermore, all DGs are designed to have active power outputs ranging between 0 and 2 MW, and reactive power outputs between 0 and 2 MVAr, respectively. Note that these values also define the bounding rectangle for the DGs within the third DS.

5.2. Dataset generation, training, and approximation quality in ML models

To develop the ML models, the first step involves generating the dataset, for which we employ LHS, as detailed earlier. For the first DS, a total of 20,000 data points are generated, while 100,000 data points are generated for both the second and third DSs. It is important to note that, as previously discussed, the same dataset and ML models are used for both the second and third DSs to demonstrate that the proposed method

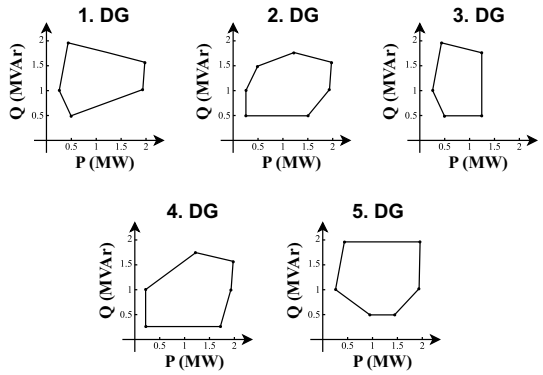

Fig. 6. Convex polygon PQ characteristics for DGs in the third DS.

maintains high performance, irrespective of the specific PQ characteristics. After generating the datasets, we train our ML models by following standard procedures for both classification and regression tasks. The dataset is divided into a training set (80%) and a test set (20%) to validate the model's performance. In addition, the hyperparameters of the NN models are optimized using k-fold cross-validation applied to the training set.

We employ NN classification models to distinguish between feasible and infeasible operating points based on the generated $\boldsymbol{x}_j$ values. For constructing these NN models, we employ random search hyperparameter tuning, selecting $n_{\mathrm{h},1} = 20$ hidden nodes for the first DS, and $n_{\mathrm{h},2} = 1,000$ and $n_{\mathrm{h},3} = 1,000$ hidden nodes for the second and third DSs, respectively. As the complexity of the power system increases, the number of facets required to accurately represent the feasible space of the DSs also rises, hence the increased number of hidden nodes. It is important to recall that the number of hidden nodes, $n_{\mathrm{h},j}$, provides an upper bound on the number of facets that define the polytope. Consequently, some rows of the matrix W_j and vector b_j may be redundant. Therefore, even when a large number of hidden nodes are defined, the NN only generates as many facets as necessary to describe the feasible region effectively.

After training the classification models, we assess their approximation quality by evaluating them on the test sets. Let $y_i \in \{0, 1\}$ denote the true feasibility status of instance i, where $y_i = 0$ indicates a feasible instance and $y_i = 1$ indicates an infeasible instance. Let $\tilde{y}_i$ denote the feasibility status determined by the model $FR_j(\cdot)$. For a dataset containing N instances, the performance of $FR_j(\cdot)$ is evaluated using the accuracy, recall, and specificity metrics [46].

The accuracy is defined as the fraction of instances for which the determined feasibility status matches the true status:

$$\text{Accuracy} = \frac{1}{N}\sum_{i=1}^{N} \mathbf{1}\left(\tilde{y}_i = y_i\right). \tag{9}$$

The recall measures the fraction of feasible instances that are correctly identified:

$$\text{Recall} = \frac{\sum_{i=1}^{N} \mathbf{1}\left(\tilde{y}_i = 0 \wedge y_i = 0\right)}{\sum_{i=1}^{N} \mathbf{1}\left(y_i = 0\right)}. \tag{10}$$

The specificity measures the fraction of infeasible instances that are correctly identified:

$$\text{Specificity} = \frac{\sum_{i=1}^{N} \mathbf{1}\left(\tilde{y}_i = 1 \wedge y_i = 1\right)}{\sum_{i=1}^{N} \mathbf{1}\left(y_i = 1\right)}. \tag{11}$$

Here, $\mathbf{1}(\cdot)$ denotes the indicator function, which equals 1 when the condition holds and 0 otherwise. The results are summarized in Table 1.

Table 1
Accuracy, recall and specificity metrics of the NN models.

Model	Accuracy	Recall	Specificity
$FR_1(\boldsymbol{x}_1)$	99.90%	99.89%	100.00%
$FR_2(\boldsymbol{x}_2)$ & $FR_3(\boldsymbol{x}_3)$	96.47%	97.23%	95.53%

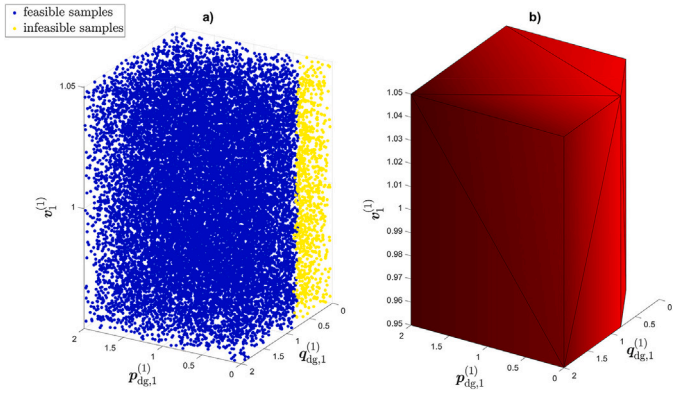

Fig. 7. a) Dataset indicating feasible and infeasible samples. b) Feasible region approximation of the NN indicating the facets.

For the NN model of the first DS, i.e., $FR_1(\boldsymbol{x}_1)$, which is a relatively less complex system, the all metrics are observed to be nearly 100%. Additionally, Fig. 7 provides a visual representation of the generated dataset and the NN's approximation of the feasible region for the first DS. Notably, if the voltage were assumed to be constant, the feasible region would be represented as a two-dimensional area. However, the figure illustrates a larger three-dimensional region, demonstrating that incorporating voltage variations allows for better utilization of DS flexibility potential. As depicted in Fig. 7, the NN model accurately approximates the feasible region and successfully establishes a well-defined decision boundary.

When examining the models for the second and third DS, i.e., $FR_2(\boldsymbol{x}_2)$ and $FR_3(\boldsymbol{x}_3)$, it is observed that the accuracy and recall metrics are 96.47% and 97.23%, respectively, while the specificity metric is 95.53%. These results indicate that, although the NN achieves high performance even for complex DSs, it does not reach 100%. In particular, the specificity metric reflects the model's ability to correctly classify infeasible samples. Misclassifying infeasible points as feasible can pose serious risks in power system operation, highlighting the importance of the conservativeness parameter introduced in Eq. (7). This parameter is therefore critical in ensuring reliable system operation, and its impact will be further analyzed in the following section.

Following the NN-based classification models, we develop quadratic regression models and evaluate their performance using the root mean squared error (RMSE) and the mean absolute error (MAE). Let z_i denote the true value (i.e., real or reactive power flow at a PCC) for instance i, and let $\tilde{z}_i$ denote the value determined by the regression model (i.e., $P_{j,u}(\cdot)$ or $Q_{j,u}(\cdot)$). Then, the RMSE and MAE are defined as:

$$\text{RMSE} = \sqrt{\frac{1}{N}\sum_{i=1}^{N} (\tilde{z}_i - z_i)^2}. \tag{12}$$

$$\text{MAE} = \frac{1}{N}\sum_{i=1}^{N} \left|\tilde{z}_i - z_i\right|. \tag{13}$$

RMSE penalizes larger deviations more strongly due to the squared term, whereas MAE measures the average magnitude of the deviations. The results, displayed in Table 2, indicate that all regression models achieved almost perfect performance. These numerical results clearly

Table 2
RMSE and MAE metrics of the quadratic regression models.

Model	RMSE	MAE
$P_{1,1}(\boldsymbol{x}_1)$	5.0×10^{-4}	3.6×10^{-4}
$P_{2,1}(\boldsymbol{x}_2)$ & $P_{3,1}(\boldsymbol{x}_3)$	2.9×10^{-4}	2.0×10^{-4}
$P_{2,2}(\boldsymbol{x}_2)$ & $P_{3,2}(\boldsymbol{x}_3)$	4.9×10^{-4}	3.4×10^{-4}
$Q_{1,1}(\boldsymbol{x}_1)$	4.3×10^{-4}	3.0×10^{-4}
$Q_{2,1}(\boldsymbol{x}_2)$ & $Q_{3,1}(\boldsymbol{x}_3)$	2.7×10^{-4}	1.8×10^{-4}
$Q_{2,2}(\boldsymbol{x}_2)$ & $Q_{3,2}(\boldsymbol{x}_3)$	4.5×10^{-4}	3.1×10^{-4}

demonstrate that the ML models are highly effective in capturing and mapping the characteristics of the DSs.

5.3. Analysis of the impact of the conservativeness parameter

After constructing the ML models, it is essential to examine the effect of the conservativeness parameter defined in Eq. (7), as this parameter directly mitigates the risk of misclassification. This analysis should first be conducted from the perspective of the DSOs responsible for generating the ML models. As discussed in the previous sections, the parameters $A_{\mathrm{FR},j}$ and $b_{\mathrm{FR},j}$ are derived from the NN parameters W_j and b_j. Once these values are obtained, the influence of different values of $c_{\mathrm{FR},j}$ can be systematically examined by substituting the corresponding $\boldsymbol{x}_j$ samples from the test set (generated in the previous section) into Eq. (7). The outcomes are then assessed using the relevant performance metrics, with the results presented in Fig. 8.

As expected, increasing $c_{\mathrm{FR},j}$ shifts the polytope's boundary inward, leading to an improvement in the specificity metric. This indicates that the model becomes more effective at avoiding the critical misclassification of infeasible points as feasible, which is the desired outcome. Conversely, the recall metric decreases with larger values of $c_{\mathrm{FR},j}$, reflecting a reduction in the model's ability to correctly identify feasible points. This decline corresponds to the loss of feasible space, thereby highlighting the inherent trade-off between conservativeness and the completeness of the feasible region representation.

The impact of the conservativeness parameter on system cost should be assessed from the perspective of the TSO, once the ML models are transferred. To this end, both the feasibility and the total cost of the system are evaluated under varying values of $c_{\mathrm{FR},j}$. Specifically, the proposed method is benchmarked against the standard AC-OPF formulation across 1000 randomly generated sets of cost coefficients using the created power system. In this comparison, the proposed method is implemented using (4), while the benchmark AC-OPF solution is obtained from (1). The results, presented in Fig. 9, illustrate the effect of the conservativeness parameter relative to the AC-OPF reference,

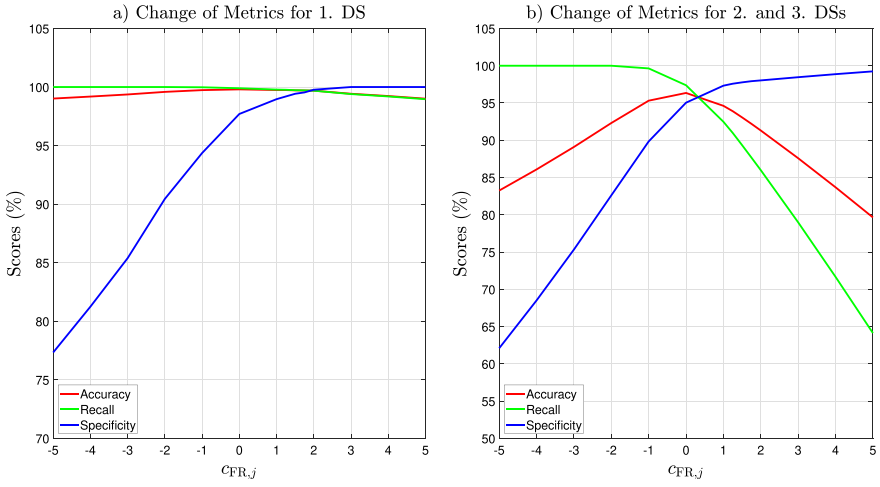

Fig. 8. Change of metrics according to the conservativeness parameter.

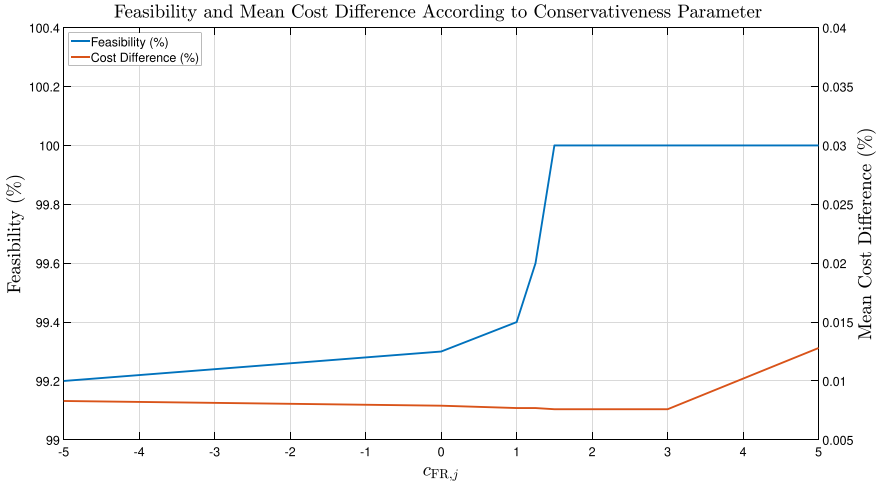

Fig. 9. Feasibility and mean cost difference according to the conservativeness parameter, taking AC-OPF as the reference.

Table 3
Metrics of the NN models under constant PCC voltage.

Model	Accuracy	Recall	Specificity
$FR_1(\boldsymbol{x}_1)$	100.00%	100.00%	100.00%
$FR_2(\boldsymbol{x}_2)$ & $FR_3(\boldsymbol{x}_3)$	99.58%	99.85%	99.18%

highlighting the trade-offs between feasibility and total system cost.

Feasibility increases with higher values of $c_{\mathrm{FR},j}$, reaching 100% once this parameter exceeds approximately 1.5. In other words, the proposed method consistently identifies operating points that remain feasible within the standard AC-OPF. This outcome underscores the effectiveness of prioritizing the avoidance of infeasible operating points, albeit at the expense of a slight increase in total cost. Notably, the mean cost difference does not rise sharply as feasibility improves; rather, the increase becomes more pronounced only beyond a certain threshold of $c_{\mathrm{FR},j}$. From a practical perspective, this suggests that the TSO and DSO may prioritize feasibility and select $c_{\mathrm{FR},j}$ values that ensure 100% feasibility, while still accounting for the system's operational and economic conditions when determining the final choice.

5.4. Analysis of the impact of the varying voltage at the PCCs

In this subsection, we investigate the impact of varying PCC voltages on the proposed methodology. To isolate this effect, all parameters described previously, such as the power system configuration, dataset size, and other modeling assumptions, are kept constant, while only the PCC voltages (i.e., $\boldsymbol{v}_j$) are excluded from the variable set $\boldsymbol{x}_j$, and the entire process is repeated. Unlike the general approach adopted throughout the paper, the dataset in this case is generated by fixing the PCC voltages at 1 p.u. The resulting NN performance metrics are summarized in Table 3.

An examination of the NN metrics reveals that the models perform better when PCC voltages are held constant compared to the case with varying voltages. This outcome is fundamentally expected, as fixing the PCC voltages reduces the dimensionality of the NN input space, thereby simplifying the learning task. Furthermore, the quadratic regression models also demonstrate consistently strong performance, with all results approaching 100%. For brevity, these numerical values are not included in a table.

Subsequently, the constructed model is transferred to the TSO, as in the previous section, and the proposed method is solved for 1000 different sets of cost coefficients. The results are then compared with the standard AC-OPF in which the PCC voltage is not fixed, and the comparison is presented in the form of histograms in Fig. 10(a). In addition, for a more detailed comparison, the case with varying PCC voltages (taken from the Section 5.3) is also benchmarked against AC-OPF, with the results shown in Fig. 10(b). For a fair comparison between the two cases, the conservativeness parameter is set to $c_{\mathrm{FR},j} = 2$ in both scenarios.

Note that, feasibility reaches 100% in both cases. As shown in Fig. 10, the average and maximum cost differences for the varying-voltage case are 0.0076% and 0.2794%, respectively, whereas these values increase to 1.638% and 4.7924% when the PCC voltage is fixed. This finding indicates that, although NN models achieve higher predictive performance in the constant-voltage case, the resulting cost differences compared to AC-OPF are significantly larger. Consequently, allowing PCC voltages to vary enables a more cost-effective utilization of DS flexibility. This underscores the critical role of voltage variability at PCCs in improving the economic efficiency of the proposed method.

5.5. Computational time performance of the proposed method

Another important criterion for evaluating the effectiveness of the proposed method is its computational performance. In this regard, the case with $c_{\mathrm{FR},j} = 2$, examined in Section 5.3, is compared against the standard AC-OPF in terms of solution time, with the results illustrated as a histogram in Fig. 11.

The analysis shows that the average time difference is only 0.0647 s, with a maximum difference of 0.2594 s, highlighting the minimal computational overhead introduced by the proposed method. Negative time differences correspond to cases where the proposed method is faster, and indeed, several instances demonstrate improved speed relative to standard AC-OPF. This efficiency can be attributed to the tailored NN architecture embedded in the framework, which enhances computational speed while preserving accuracy. Overall, the proposed method provides privacy-preserving solutions with negligible time difference compared to AC-OPF.

5.6. Scalability analysis of the proposed method

To demonstrate the scalability performance of the proposed method, we construct a larger test system consisting of a 162-bus TS interconnected with three 136-bus DSs. Each DS in this setup includes 10 DGs. For consistency and brevity, the same parameter settings, dataset sizes, and PCC bus numbers as in the previous cases are adopted. Furthermore, to assess the method's performance under diverse FPU characteristics, we employ the convex polygon PQ characteristics illustrated in Fig. 6, with each characteristic type assigned to two DGs. These characteristics

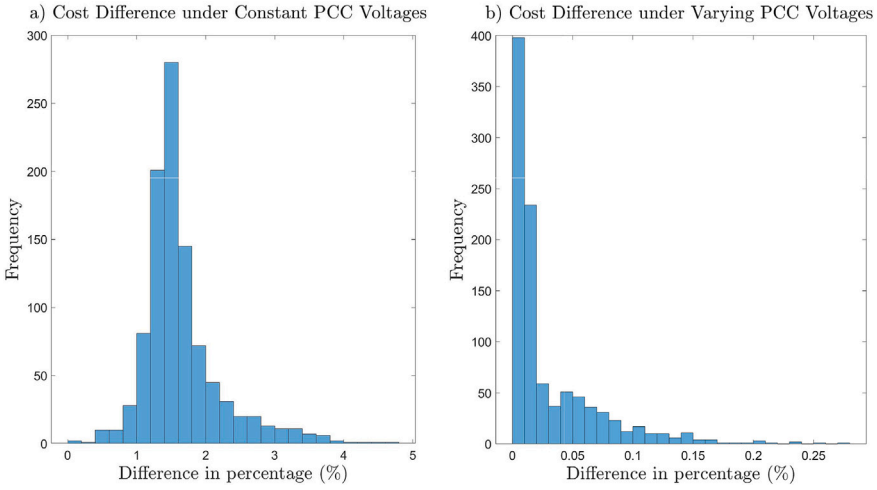

Fig. 10. Cost difference comparison under varying and constant PCC voltages.

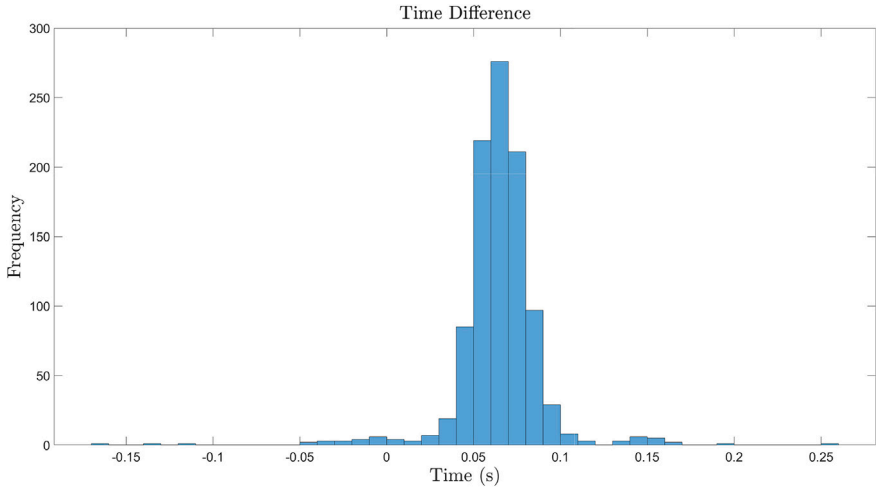

Fig. 11. Histogram of the computational time differences taking AC-OPF as the reference.

Table 4
Metrics of the NN models for scalability analysis.

Model	Accuracy	Recall	Specificity
$FR_1(\boldsymbol{x}_1)$	98.03%	96.17%	98.91%
$FR_2(\boldsymbol{x}_2)$ & $FR_3(\boldsymbol{x}_3)$	97.04%	96.39%	97.37%

are mathematically represented as sets of linear inequalities, as defined in (3).

Following the construction of this extended power system, the datasets are generated and the ML models are trained. The performance metrics of the NN models are presented in Table 4. Despite the increased number of busbars and DGs, the NN models maintain high accuracy. It is important to note that these results correspond to the case where $c_{\mathrm{FR},j} = 0$; as discussed earlier, the specificity metric can be further improved by appropriately tuning $c_{\mathrm{FR},j}$. Similarly, the quadratic regression models again achieve performance levels close to 100%, and for brevity these values are not reported in a separate table.

Subsequently, the trained models are transferred to the TSO, which applies the proposed method across 1000 randomly generated sets of cost coefficients with $c_{\mathrm{FR},j} = 2$. The results, shown in Fig. 12, compare the proposed method with the standard AC-OPF in terms of both cost difference and computational time.

In this scalability study, the proposed method again achieves 100% feasibility. When examining the cost performance, the mean cost difference is 0.36%, while the maximum cost difference is 0.72%. This demonstrates the efficiency of the proposed method in terms of cost. In terms of computational performance, the average time difference is 0.1 s, with a maximum of 0.39 s, further confirming the computational efficiency of the approach. These results highlight that the proposed framework remains both accurate and efficient even in large-scale, meshed TS–DS systems.

Moreover, the proposed method effectively accommodates diverse FPU characteristics while maintaining strong performance. Given that different FPU characteristics are treated as constraints, this approach demonstrates the capacity to incorporate other potential market-based or operational constraints between TSOs and DSOs without any loss in performance. Consequently, the proposed method achieves a balance between data privacy and operational efficacy, yielding comparable performance to the standard AC-OPF. This capability enables DS flexibility to be leveraged for network management purposes without compromising data privacy.

6. Conclusion

With the transformation of the power system, distribution systems (DSs) are playing an increasingly crucial role, accompanied by a growing number of flexibility-providing units (FPUs). Leveraging the flexibility

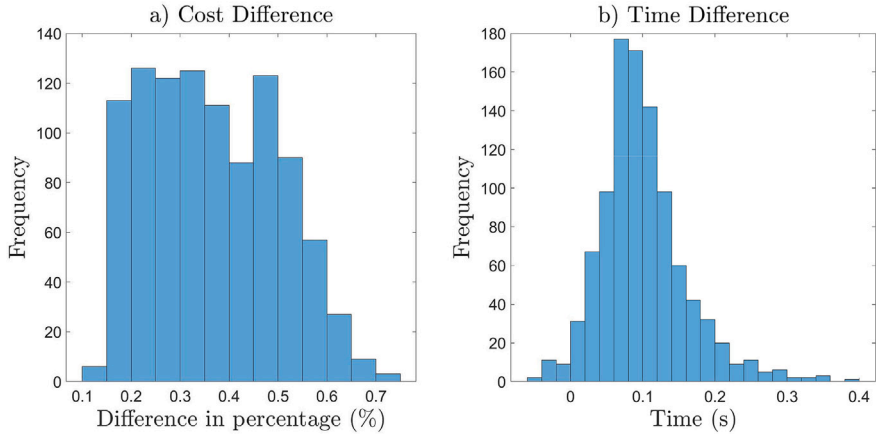

Fig. 12. Histogram of total cost and computational time differences for scalability analysis, with AC-OPF taken as the reference.

offered by DSs has become essential for ensuring that network management is both cost-effective and secure. Achieving this requires seamless interoperability among network stakeholders, including Transmission System Operators (TSOs) and Distribution System Operators (DSOs). However, concerns regarding the disclosure of sensitive information, such as network topology and customer load profiles, hinder this interoperability and impede effective network management.

In this context, we propose a machine learning (ML)-based method in the present paper that prevents sensitive data from circulating between stakeholders, thereby enhancing interoperability across the network. In our approach, we represent the technical constraints of the DSs using ML models, which can be shared with the TSO without compromising data privacy. By leveraging these ML models, the TSO can solve the optimal power flow (OPF) problem and directly determine the dispatch of FPUs. This allows for dispatch decisions to be made in a single round of communication, eliminating the need for an additional disaggregation step. Furthermore, we demonstrate the method's flexibility by applying it to FPUs with a variety of PQ characteristics, not limited to ideal rectangular PQ charts, indicating that the method is adaptable to diverse FPU characteristics. Additionally, the flexibility potential of DSs is leveraged more effectively by accounting for variations at points of common coupling (PCCs) voltage. Moreover, to accurately represent the feasible region of the DSs, we propose a novel, tailored neural network (NN) architecture that performs this task with high computational efficiency.

The proposed method is benchmarked against the standard AC-OPF using multiple DSs with meshed connections and multiple PCCs. The results demonstrate high performance in terms of ML accuracy and overall effectiveness, highlighting the capability of the proposed method to protect data privacy while achieving reliable results. By modeling DSs with ML models, the TSO is prevented from accessing sensitive DS information, allowing the flexibility from DSs to be leveraged in network management without compromising data privacy. This approach thus promotes interoperability among stakeholders and enables more effective and secure network management.

Furthermore, a promising direction for future research is to benchmark the proposed method against other mainstream privacy-preserving approaches, such as differential privacy and distributed OPF, focusing on key aspects including communication overhead, convergence behavior, feasibility guarantees, and the level of privacy protection.

Another important direction for future work is to extend the proposed framework to explicitly account for changing operating conditions in DSs. In practice, the feasible operating region of a DS may vary due to fluctuations in load levels, renewable generation, or network topology modifications. While the proposed NN-based feasible region representation is trained over a broad operating domain and demonstrates consistent performance across DSs with different sizes and structures, incorporating uncertainty-aware or topology-adaptive learning mechanisms could further enhance the generalization capability of the model.

CRediT authorship contribution statement

Burak Dindar: Writing – original draft, Visualization, Software, Resources, Methodology, Investigation, Formal analysis, Data curation, Conceptualization. **Can Berk Saner:** Writing – original draft, Visualization, Software, Resources, Methodology, Investigation, Formal analysis, Data curation, Conceptualization. **Hüseyin K. Çakmak:** Writing – review & editing, Visualization, Validation, Supervision, Project administration, Funding acquisition. **Veit Hagenmeyer:** Writing – review & editing, Validation, Supervision, Project administration.

Declaration of competing interests

The authors declare that they have no known competing financial interests or personal relationships that could have appeared to influence the work reported in this paper.

Acknowledgements

This work was conducted within the framework of the Helmholtz Program Energy System Design (ESD 37.12.02) and the DigIPlat project, which received funding within the framework of the joint programming initiative ERA-Net Smart Energy Systems' focus initiative Digital Transformation for the Energy Transition, with support from the European Union's Horizon 2020 research and innovation program under grant agreement No. 883973.

Data availability

Data will be made available on request.

References

[1] Jia H, Qi W, Liu Z, Wang B, Zeng Y, Xu T. Hierarchical risk assessment of transmission system considering the influence of active distribution network. IEEE Trans Power Syst 2014;30(2):1084–93.
[2] Ringelstein J, Vogt M, Khavari AM, Ciavarella R, Di Somma M, Graditi G. A methodology for improved TSO-DSO coordination in grid operation planning. Electr Power Syst Res 2022;211:108445.
[3] Gerard H, Rivero E, Six D. Basic schemes for TSO-DSO coordination and ancillary services provision. SmartNet Deliv D 2016;1:12.
[4] Givisiez AG, Petrou K, Ochoa LF. A review on TSO-DSO coordination models and solution techniques. Electr Power Syst Res 2020;189:106659.
[5] Dai X, Guo Y, Jiang Y, Jones CN, Hug G, Hagenmeyer V. Real-time coordination of integrated transmission and distribution systems: flexibility modeling and distributed NMPC scheduling. Electr Power Syst Res 2024;234:110627.
[6] Lind L, Cossent R, Frías P. Evaluation of TSO–DSO coordination schemes for meshed-to-meshed configurations: lessons learned from a realistic Swedish case study. Sustain Energy Grids Netw 2023;35:101125.
[7] Migliavacca G. TSO-DSO interactions and ancillary services in electricity transmission and distribution networks: modeling, analysis and Case-Studies. Springer; 2019.
[8] Ziesemann C, Gaumnitz F, Köhnen CS, Stoyanova IE. Challenges and barriers to the implementation of TSO-DSO coordination concepts: discussion paper. Universitätsbibliothek der RWTH Aachen; 2023.
[9] Habibi M, Vahidinasab V, Sepasian MS. A privacy-preserving approach to day-ahead TSO-DSO coordinated stochastic scheduling for energy and reserve. IET Gener Transm Distrib 2022;16(1):163–80.
[10] Mak TWK, Fioretto F, Shi L, Van Hentenryck P. Privacy-preserving power system obfuscation: a bilevel optimization approach. IEEE Trans Power Syst 2019;35(2):1627–37.
[11] Fioretto F, Mak TWK, Van Hentenryck P. Differential privacy for power grid obfuscation. IEEE Trans Smart Grid 2019;11(2):1356–66.
[12] Mak TWK, Fioretto F, Van Hentenryck P. Privacy-preserving obfuscation for distributed power systems. Electr Power Syst Res 2020;189:106718.
[13] Fioretto F, Van Hentenryck P. Constrained-based differential privacy: releasing optimal power flow benchmarks privately: releasing optimal power flow benchmarks privately. In: Integration of constraint programming, artificial intelligence, and operations research: 15th international conference, CPAIOR 2018, delft, the netherlands, June 26–29, 2018, proceedings 15. Springer; 2018. p. 215–31.
[14] Dai X, Zhai J, Jiang Y, Guo Y, Jones CN, Hagenmeyer V. Advancing distributed AC optimal power flow for integrated transmission-distribution systems. IEEE Trans Netw Sci Eng 2025;12(2):1210–23.
[15] Jiang T, Wu C, Zhang R, Li X, Li F. Risk-averse TSO-DSOs coordinated distributed dispatching considering renewable energy and demand response uncertainties. Appl Energy 2022;327:120024.
[16] Dai X, Kocher A, Kovačević J, Dindar B, Jiang Y, Jones C, Çakmak HK, Hagenmeyer V. Ensuring data privacy in AC optimal power flow with a distributed co-simulation framework. Electr Power Syst Res 2024;235:110710.
[17] Silva J, Sumaili J, Bessa RJ, Seca L, Matos MA, Miranda V, Caujolle M, Goncer B, Sebastian-Viana M. Estimating the active and reactive power flexibility area at the TSO-DSO interface. IEEE Trans Power Syst 2018;33(5):4741–50.
[18] Capitanescu F. TSO–DSO interaction: active distribution network power chart for TSO ancillary services provision. Electr Power Syst Res 2018;163:226–30.
[19] Churkin A, Kong W, Gutierrez JNM, Ceseña EAM, Mancarella P. Tracing, ranking and valuation of aggregated DER flexibility in active distribution networks. IEEE Trans Smart Grid 2023;15(2):1694–711.
[20] Wang S, Wu W. Aggregate flexibility of virtual power plants with temporal coupling constraints. IEEE Trans Smart Grid 2021;12(6):5043–51.
[21] Contreras DA, Rudion K. Time-based aggregation of flexibility at the TSO-DSO interconnection point. In: 2019 IEEE PES gen. Meet. IEEE; 2019. p. 1–5.
[22] Vijay R, Mathuria P. Complex power flexibility evaluation using energy arbitrage between transmission and distribution. Electr Power Syst Res 2022;203:107641.
[23] Fortenbacher P, Demiray T. Reduced and aggregated distribution grid representations approximated by polyhedral sets. Int J Electr Power Energy Syst 2020;117:105668.
[24] Usman M, Alizadeh MI, Capitanescu F, Avramidis I-I, Madureira AG. A novel two-stage TSO–DSO coordination approach for managing congestion and voltages. Int J Electr Power Energy Syst 2023;147:108887.

[25] Sarstedt M, Hofmann L. Monetarization of the feasible operation region of active distribution grids based on a cost-optimal flexibility disaggregation. IEEE Access 2022;10:5402–15.
[26] Chen X, Li N. Leveraging two-stage adaptive robust optimization for power flexibility aggregation. IEEE Trans Smart Grid 2021;12(5):3954–65.
[27] Polymeneas E, Meliopoulos S. Aggregate modeling of distribution systems for multi-period OPF. In: Power Syst. Comput. Conf. (PSCC). IEEE; 2016. p. 1–8.
[28] Früh H, Müller S, Contreras D, Rudion K, von Haken A, Surmann B. Coordinated vertical provision of flexibility from distribution systems. IEEE Trans Power Syst 2022;38(2):1834–44.
[29] Kalantar-Neyestanaki M, Sossan F, Bozorg M, Cherkaoui R. Characterizing the reserve provision capability area of active distribution networks: a linear robust optimization method. IEEE Trans Smart Grid 2019;11(3):2464–75.
[30] Riaz S, Mancarella P. Modelling and characterisation of flexibility from distributed energy resources. IEEE Trans Power Syst 2021;37(1):38–50.
[31] Tan Z, Zhong H, Xia Q, Kang C, Wang XS, Tang H. Estimating the robust PQ capability of a technical virtual power plant under uncertainties. IEEE Trans Power Syst 2020;35(6):4285–96.
[32] Stock DS, Sala F, Berizzi A, Hofmann L. Optimal control of wind farms for coordinated TSO-DSO reactive power management. Energies 2018;11(1):173.
[33] Xu Y, Yao L, Pu T, Liao S, Cheng F, Li Y, Wang X. Voltage-dependent PQ reserve capacity evaluation at TSO-DSO interface considering uncertainties of DGs and FLs. CSEE J Power Energy Syst 2022;10(5):1935–54.
[34] Dindar B, Saner CB, Çakmak HK, Hagenmeyer V. TSO-DSO interaction: privacy-preserving optimal power flow with distributed generators using a machine learning-based approach. In: IEEE PES 15th Asia-Pacific power energy eng. conf. (APPEEC). IEEE; 2023. p. 1–6.
[35] Dindar B, Saner CB, Polat DY, Çakmak HK, Hagenmeyer V. A machine learning-based privacy-preserving approach to incorporate distributed generators in AC optimal power flow. In: 2024 IEEE PES innov. smart grid technol. Conf. Europe (ISGT-europe). IEEE; 2024. p. 1–6.
[36] ENTSO-E. Towards smarter grids: developing TSO and DSO roles and interactions for the benefit of consumers, Availabe: 2015. https://eepublicdownloads.entsoe.eu/clean-documents/Publications/Position%20papers%20and%20reports/150303_ENTSOE_Position_Paper_TSO-DSO_interaction.pdf
[37] Huntington D, Lyrintzis CS. Improvements to and limitations of latin hypercube sampling. Probabilistic Eng Mech 1998;13(4):245–53.
[38] Schneider DAC. Estimation of flexibility potentials in active distribution networks, vol. 34. BoD–Books on Demand; 2021.
[39] Riaz S, Mancarella P. On feasibility and flexibility operating regions of virtual power plants and TSO/DSO interfaces. In: 2019 IEEE milan PowerTech. IEEE; 2019. p. 1–6.
[40] Contreras DA, Rudion K. Computing the feasible operating region of active distribution networks: comparison and validation of random sampling and optimal power flow based methods. IET Gener Transm Distrib 2021;15(10):1600–12.
[41] Liu B, Liu F, Wei W, Wang J. Estimating B-coefficients of power loss formula considering volatile power injections: an enhanced least square approach. IET Gener Transm Distrib 2018;12(12):2854–60.
[42] Zimmerman RD, Murillo-Sánchez CE, Thomas RJ. Matpower: steady-state operations, planning, and analysis tools for power systems research and education. IEEE Trans Power Syst 2011;26(1):12–19. https://doi.org/10.1109/TPWRS.2010.2051168
[43] Byrd RH, Nocedal J, Waltz RA. Knitro: an integrated package for nonlinear optimization. Large-scale nonlinear optimization 2006:35–59.
[44] Abadi M, et al. TensorFlow: large-scale machine learning on heterogeneous systems, software available from tensorflow.org 2015. https://www.tensorflow.org/
[45] Chollet F, et al. Keras, 2015. https://keras.io
[46] Hossin M, Sulaiman MN. A review on evaluation metrics for data classification evaluations. Int J Data Min Knowl Manag Process 2015;5(2):1.